Journal of Zhejiang University-SCIENCE A (Applied Physics & Engineering) 2022 23(5):358-374
www.jzus.zju.edu.cn; www.springer.com/journal/11582
E-mail: jzus_a@zju.edu.cn

Research Article

https://doi.org/10.1631/jzus.A2100487

An analytical investigation of the collapse of asymmetrically corroded pipes under external pressure

Sun-ting YAN✉, Ping TANG, Zhang-wei LING, Yong-gui CHEN

Zhejiang Academy of Special Equipment Science, Hangzhou 310020, China

Abstract: This paper presents an analytical investigation of elastic collapse of asymmetrically corroded rings under external pressure when both internal corrosion and external corrosion exist. Governing equations are derived for membrane inextensible and membrane extensible cases; a full continuity condition is rigorously derived by the Euler-Bernoulli beam assumption. Comparison with finite element analysis (FEA) shows good agreement for load-displacement curves but membrane extensibility should be included to accurately predict the initial deformation phase, although the discrepancy for both the inextensible and extensible models vanishes for larger deformation phases. By the perturbation technique, the initial load-displacement slope is calculated, and extensive parametric analysis shows complicated dependency of this slope on the misalignment parameter and the angular extent of corrosion. We also present an infallible semi-analytical perturbation solution for both homogeneous and inhomogeneous cases by the Lyapunov arbitrary small-parameter method and show that the resulting power series always converges; then a mathematical argument of analyticity has been presented to illustrate that the so-called homotopy analysis method in the literature converges when the convergence controlling parameter is lying in (−2, 0). This paper serves to enhance the understanding of asymmetrically corroded rings and it is mainly relevant to offshore engineering.

Key words: Pipe; Corrosion; Analytical method; External pressure; Perturbation method

1 Introduction

Subsea pipelines under external pressure may collapse by local buckling and subsequent buckle propagation. The buckling propagation may cause the entire pipeline to fail and cause significant economic loss. The intact subsea pipeline collapse under external pressure, bending moment, and axial tension is treated in detail in (Kyriakides and Corona, 2007). However, in a hostile environment, the pipeline may be corroded internally and externally by corrosive fluid and sea water. The effect of corrosion on pipeline integrity has attracted much research. Through an experimental and numerical treatment (Netto et al., 2007; Netto, 2009) the pit corrosion defect and the long but narrow corrosion defect were studied and empirical formulas to predict the critical collapse pressure were derived. By extensive finite element analysis (FEA) simulation, the collapse failure and capacity of subsea pipelines with complex corrosion defects were studied (Chen et al., 2021a, 2021b). Based on the data, an empirical prediction formula was derived. When there are several coexisting corrosion defects, their interaction effect is significant and so an experiment for pipes with two circumferential or axial defects was conducted, and an empirical formula for elliptic defect was presented (Gong et al., 2020, 2021). An FEA simulation of pipe collapse was conducted (Yan et al., 2016; Ye et al., 2016) with a rectangular corrosion defect under combined axial tension and pressure. The tension was shown to reduce the collapse pressure. The empirical formula is in great agreement with numerical data. Sandwich pipes with corrosion defects have also been numerically investigated (Shen et al., 2016). The above analysis does not involve randomness of corrosion defects and so FEA simulation with random parameters was conducted (Yu et al., 2017). A comparison analysis of the feasibility of empirical formulas derived in literature has been carried out

✉ Sun-ting YAN, yansunting@zju.edu.cn
Sun-ting YAN, https://orcid.org/0000-0001-9939-916X

Received Sept. 30, 2021; Revision accepted Oct. 18, 2021;
Crosschecked Mar. 30, 2022

by Teixeira et al. (2019) and many collapse models have been compared (Netto et al., 2007; Netto, 2009).

The above research is primarily based on numerical and experimental work, but recently some related theoretical studies have been conducted to represent the pipe by a 2D ring model. Based on a theoretical ring model, Fatt (1999) studied the elastic bifurcation pressure and plastic collapse pressure of a locally corroded ring. The bifurcation pressure of locally corroded pipelines assuming uniform corrosion depth was studied by Xue and Fatt (2002) and Xue (2008). Similar analytical investigations for pipe collapse with material circumferential inhomogeneity under external pressure were conducted by Fraldi and Guarracino (2011, 2013) and the tangent modulus method was used to represent the plasticity. The elastic and elastoplastic collapse of corroded rings and a non-uniform curved shallow arch were studied analytically (Yan et al., 2015, 2016, 2017, 2018a, 2018b, 2018c).

Very recently, through a solution of an eigenvalue problem by extending the solution of the work of Yan et al. (2016), the elastic-plastic buckling of pipes with the so-called asymmetric local wall thinning was studied (Wu et al., 2021), where internal corrosion and external corrosion have different depths through considering moment jump at discontinuity cross-section. Also recently, a semi-analytical approach by the so-called homotopy analysis method developed by Liao (2009, 2012) has been used to analytically solve for the bifurcation pressure of non-uniformly corroded rings through a solution of an eigenvalue problem by Chen et al. (2021a).

However, the corrosion defects represent some geometric imperfections and thus this is not strictly an eigenvalue problem of a homogeneous equation. The eigenvalue solution just presents an upper bound on collapse pressure and does not offer any information on complicated deformation when pressure is increasing from zero. Thus, no stress information can be obtained.

In this paper, we develop inhomogeneous governing equations (when the inhomogeneous term is dropped, it becomes the same homogeneous equation as in the work of Wu et al. (2021)) on an asymmetrically corroded ring to study the effect of the misalignment parameter e on the deformations. By rigorously adopting the Euler-Bernoulli beam assumptions, we present two sets of continuity conditions and show that these two continuity conditions lead to a very slight difference in critical pressure prediction. We develop a perturbation solution for the initial slope prediction of load-displacement curves when the misalignment parameter e is varying and we study the effects of corrosion angular extent and of corrosion depth. We propose an alternative semi-analytical solution, using the Lyapunov arbitrary small-parameter method, to allow analytical calculation for both the homogeneous equation and the inhomogeneous equation of ring collapse. By a mathematical inequality, we conclude that the convergence of power series is guaranteed with infinite convergence radius. We also present a discussion on the effect of the so-called convergence controlling parameter c_0 in the homotopy analysis method and an interesting mathematical argument of analyticity has shown that this parameter should lie in (−2, 0) to guarantee the convergence of the power series.

This paper is organized as follows: in Section 2, we present the governing equations, related boundary and continuity conditions and also present the initial slope calculation method. In Section 3, a comparison with FEA is presented to verify the accuracy of theoretical model and the effect of membrane extensibility is shown to be significant for initial deformation. In Section 4, extensive parametric analysis is presented for initial slope and characteristic pressure by eigenvalue calculation. This section shows the effect of the misalignment parameter e on deformation and bifurcation pressure. In Section 5, we present the more straightforward Lyapunov small-parameter method to solve both homogeneous and inhomogenous equations of ring collapse and conclude the convergence of power series by a mathematical estimation.

Intentionally, we move all very technical derivations to ESMs A, B, C, D, E, and F to make this paper more readable. In ESM A, we present a perturbation solution strategy for a general abstract perturbation problem and this strategy is useful in understanding the derivation of the initial slope calculation illustrated in ESM D. ESM B presents a detailed derivation of the governing inhomogeneous equation and the novel part is the rigorous treatment of rigid-body motion. ESM C presents a rigorous development of continuity conditions under the Euler-Bernoulli beam assumptions. ESM D presents detailed initial slope formulation; this process is highly non-trivial. ESM E shows mathematically that the convergence controlling parameter should be lying in (−2, 0) to guarantee

convergence of power series. ESM F presents a brief introduction of the shooting method coupled with the Newton-Raphson iteration to numerically solve the homogeneous and inhomogeneous equations in this paper. ESM G presents a simple application of elastic result derived in this paper when the plasticity effect is considered. We believe that this paper should enhance the understanding of the effect of asymmetric corrosion on collapse of pipes under external pressure.

Remark: Although this paper concerns only elastic analysis, the result from elastic analysis is generally useful enough for application. We discuss these engineering aspects here:

(1) In the case of thin pipes, collapse is generally elastic, i.e. the collapse often happens when the stress is below the yielding stress. From our previous work (Yan et al., 2016), it was shown that when the radius/thickness ratio exceeded 20, the pipeline collapsed elastically. Even for some cases where the radius/thickness ratio is merely larger than 15, the plasticity affects the collapse pressure only slightly (Figs. 4–6 in (Yan et al., 2016)). Thus, for thin pipes, the elastic collapse pressure in Section 4.2 is directly applicable.

(2) When the radius/thickness ratio is smaller than 10 (Yan et al., 2016), the plasticity effect is significant and not negligible. However, the standard practice here is to use some plasticity criterion based on pure elastic stress from the elastic solution in this paper. We note that by displacement solution and elastic constitutive relation, elastic stress is easily obtained. Historically, Timoshenko and Gere (1961) used the initial yielding criterion (failure occurs when the material initially yields) by using pure elastic solutions to obtain critical collapse pressure of a uniform ring. More involved plasticity criterion by full plasticity yielding condition has been formed by Fatt (1999) that also based on pure elastic solutions for collapse pressure of non-uniform rings (it has a similar corrosion model as this paper but deals with the special case where e=0). So Fatt (1999)'s full plasticity criterion can be used on our model without modification. We should also point out that our work differs from Fatt (1999)'s work since Fatt dealt with the symmetric corrosion case where e=0 in our notation, but we here study the more general case where e is lying in [−1, 1]. The use of a failure criterion based on pure elastic stress is a widely used practice in engineering. For example, in ASME codes (ASME, 2010), structures are said to fail if the elastic stress (from a pure elastic solution) exceeds some plasticity limits (typically defined in terms of yielding stress and tensile stress). Thus, the routine application of elastic solutions in this paper can be directly used to form some pressure criteria. ESM G shows an example of such an application.

2 Governing equations for asymmetrically corroded rings

Fig. 1 shows a schematic of a locally and asymmetrically corroded ring. The deformation is assumed to be symmetric about the middle vertical line and this 2D ring model represents well corroded pipes with long corrosion defects. To represent thickness reduction, the ring is composed of two regions: a corroded region for $s \in [0, s_1]$ and an intact region for $s \in [s_1, \pi]$ (where s_1 means the half of the angle extent of corroded region due to geometric symmetry, and s is angular coordinate). w_1, v_1 (measured with respect to the middle axis of the corroded region) and w_2, v_2 (measured with respect to the middle axis of the intact region) are the radial displacements and circumferential displacements for the corroded region and the intact region, respectively (in general, we use subscript 1 to represent variables of the corroded region and 2 to represent variables of the intact region). w_1, v_1, w_2, and v_2 are dimensional in dimension of length. t_1, R_1, t_2, and R_2 are the thicknesses and the radii of the middle axes of the corroded region and intact region,

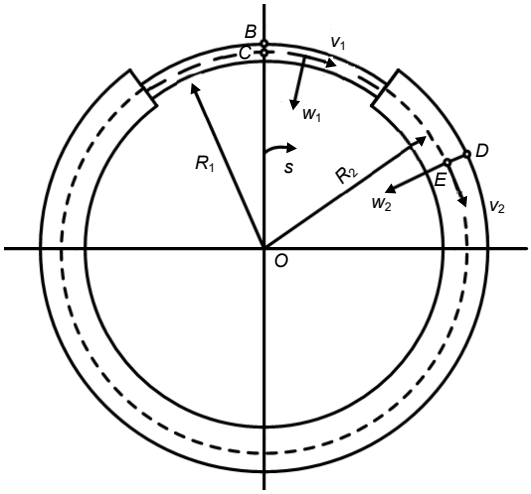

Fig. 1 Non-uniform asymmetrically corroded ring

respectively. Only a symmetric collapse mode is studied in this paper.

The external pressure p is exerted on the external surface of both corroded region and intact region, not on the middle surface. The "asymmetric" corrosion means that the middle axes of two regions may have different radii, i.e. R_1 is not necessarily equal to R_2. From derivations in ESM B, the governing equation is

$$\begin{aligned} M_1(s)+\frac{p(4R_1^2-t_1^2)}{8}-pR_1w_1(s)=\\ M_2(s)+\frac{p(4R_2^2-t_2^2)}{8}-pR_2w_2(s)=C, \end{aligned} \tag{1}$$

where C is an unknown constant and $M_1(s)$ and $M_2(s)$ are cross-section resultant moments around the middle axis point in the corroded region and the intact region, respectively.

2.1 Constitutive relationship

From the linear elastic constitutive model, M_1 and M_2 are proportional to curvature change, i.e.

$$\begin{aligned} M_1&=-(EI_1/R_1^2)(w_1''+v_1'),\\ M_2&=-(EI_2/R_2^2)(w_2''+v_2'), \end{aligned}$$

where E is the elastic modulus, I_1 and I_2 are the moments of inertia of cross-sections for corroded region and intact region, respectively, "prime" is differentiation with respect to the angular coordinate s, and the membrane strains are $(v_1'-w_1)/R_1$ and $(v_2'-w_2)/R_2$. Since the membrane stiffness is proportional to thickness while the bending stiffness is proportional to the cube of the thickness, when the thickness is small, the membrane deformation is much smaller than the bending deformation; in this case we may assume the membrane strain as zero and this is called the inextensible model in this paper. In this case, $v_1'=w_1$, $v_2'=w_2$ and then Eq. (1) is reduced to:

$$\frac{EI_i\left(w_i''+w_i\right)}{R_i^2}+pR_iw_i+\frac{p(t_i^2-4R_i^2)}{8}=C, \tag{2}$$

for i=1, 2. However, when the thickness is not small, the membrane strain is non-trivial and the extensible model by relation $Et_i(v_i'-w_i)=-pR_i(R_i+t_i/2)$, for i=1, 2, should be used. By this assumption, we can obtain:

$$\begin{aligned} v_1'&=\frac{-pR_1\left(R_1+\frac{t_1}{2}\right)}{Et_1}+w_1,\\ v_2'&=\frac{-pR_2\left(R_2+\frac{t_1}{2}\right)}{Et_2}+w_2. \end{aligned} \tag{3}$$

Then substituting Eq. (3) into the governing Eq. (1), we can obtain:

$$\begin{aligned} \frac{EI_i\left(w_i''+w_i\right)}{R_i^2}+pR_iw_i=\\ C+\frac{EI_i}{R_i^2}\frac{pR_i\left(R_i+\frac{t_i}{2}\right)}{Et_i}-\frac{p(t_i^2-4R_i^2)}{8}. \end{aligned} \tag{4}$$

Eqs. (3) and (4) give the theoretical formulation for the extensible model.

2.2 Boundary and continuity conditions

For symmetric deformation, $w_1'(0)=0$ and $w_2'(\pi)=0$, $v_1(0)=0$, and $v_2(\pi)=0$. However, as shown in ESM C for the inextensible model, rigorous use of the Euler-Bernoulli assumption would lead to complex continuity conditions at s=s_1:

$$\begin{aligned} &w_1'(s_1)=w_2'(s_1),\ \ w_1(s_1)=w_2(s_1),\\ &\frac{\int_{[0,\,s_1]}w_1\mathrm{d}s}{R_1}+\frac{\int_{[s_1,\,\pi]}w_2\mathrm{d}s}{R_2}=\frac{w_2'(s_1)}{R_2}-\frac{w_1'(s_1)}{R_1}. \end{aligned} \tag{5}$$

If $R_1=R_2$, then this leads to a simpler condition: $\int_{[0,\,s_1]}w_1+\int_{[s_1,\,\pi]}w_2=0$. This simpler continuity condition was used in the work of Wu et al. (2021), i.e.

$$\begin{aligned} &w_1(s_1)=w_2(s_1),\ \ w_1'(s_1)=w_2'(s_1),\\ &\int_{[0,\,s_1]}w_1+\int_{[s_1,\,\pi]}w_2=0. \end{aligned} \tag{6}$$

This is equivalent to assuming that there is no abrupt change of tangential displacement at s_1, i.e. $v_1(s_1)$=$v_2(s_1)$. No comparisons have been presented in the literature on the effect of these two continuity conditions; in this paper, we show, in Section 3, that these two sets of continuity conditions yield almost identical results and, as a result, we always adopt the

simpler continuity condition in Eq. (6) in calculations. For the extensible model we still adopt the simpler assumption, i.e. $v_1(s_1)=v_2(s_1)$, so now the continuity condition is:

$$w_1(s_1)=w_2(s_2),\quad w_1'(s_1)=w_2'(s_1),$$
$$\int_{[0,\,s_1]} w_1+\int_{[0,\,s_1]} w_2=\frac{pR_1\left(R_1+\frac{t_1}{2}\right)s_1}{Et_1}+ pR_2\left(R_2+\frac{t_2}{2}\right)\frac{\pi-s_1}{Et_2}. \tag{7}$$

2.3 Homogeneous version

By dropping the inhomogeneous terms in Eq. (4), the homogeneous version of the moment balance equation is:

$$\frac{EI_i\left(w_i''+w_i\right)}{R_i^2}+pR_iw_i=C,\quad i=1,\,2, \tag{8}$$

subject to boundary conditions $w_1'(0)=w_2'(\pi)=0$ and continuity equations Eq. (5) or Eq. (6). This defines an eigenvalue problem with $p=p_{cr}$ (defined as an eigenvalue) and w_i and C as eigenfunctions. The solution of this homogeneous equation is essential, since when p approaches to p_{cr} the solutions for original inhomogeneous equations in Section 2.2 are approaching infinity, as shown in ESM A.

2.4 Initial slope calculation

When p is small, Eq. (4) describes how deformation begins as p increases from zero. One might naively think to drop the term pR_iw_i since p and w_i are small and since pR_iw_i is relatively small compared with $(EI_i/R_i^2)w_i$ it could be dropped. However, it would be completely incorrect since $p=0$ is an eigenvalue of the homogeneous version of Eq. (4) and the eigenfunctions are the rigid-body displacements, i.e. $w_1=b\cos s$, $w_2=b\cos s$ for some real number b. The inhomogeneous term $EI_i/R_i^2\cdot pR_i(R_i+t_i/2)/(Et_i)-1/8\cdot p(t_i^2-4R_i^2)$ is pro-portional to p, and as $p\to 0$ it approaches to 0 as well. This is a special case of the general abstract problem of $Aw+pw=pe$, where A is some linear self-adjoint operator between some Hilbert spaces H, $e\in H$ and $w\in H$ as a solution, and there is a known $w_0\in H$ such that $Aw_0=0$. ESM A presents the general perturbative solution strategy of this problem. In ESM D, we solve this equation in detail for this special case, and it appears that this seemingly innocent problem's solution is highly non-trivial. The solution should take the following asymptotic expansion form:

$$w_i\sim c\bar{w}_{0i}+p\bar{w}_{1i}+p^2\bar{w}_{2i}+\cdots,\quad i=1,\,2,\quad p\to 0^+, \tag{9}$$

where c is a constant independent of p and $\bar{w}_{0i}=\cos s$ is just rigid-body displacement. By this result, when $p=0$, w_i is not zero but there is some constant rigid-body displacement which fact is unexpected from our perspective. Note that in the derivation process of ESM B, without loss of generality, we assume some vertical rigid body motion superimposed. This superimposition coupled with the intrinsic property of the problem $Aw+pw=pe$ in ESM A may contribute to this rigid body motion here.

3 Comparison with FEA

In this section, we present some comparisons between the above derived theoretical models and FEA results.

3.1 Finite element models

General purpose FEA software Abaqus is used and three types of geometric models are included as shown in Fig. 2.

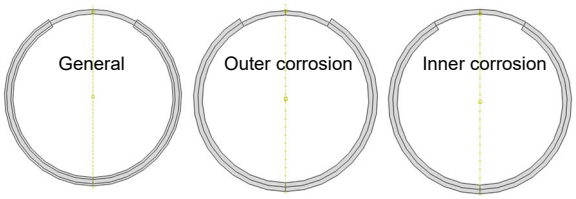

Fig. 2 Three types of geometric models

The geometric parameters are described as follows: $R_2=1$ m is fixed for all models; e is the mid-axis misalignment parameter and takes values in $[-1,\,1]$; d is the corrosion severity parameter, $d=(t_2-t_1)/t_2$ representing corrosion depth, and t_2/R_2 is the ratio of thickness t_2 to R_2 describing the thinness of the ring; s_1 is the half angular extent of the corroded region. e is defined by $R_1=e(t_2-t_1)/2+R_2$. Thus, when $e=1$, $R_1+t_1/2=R_2+t_2/2$ (i.e. the case of internal corrosion) and when

$e=-1$, $R_1-t_1/2=R_2-t_2/2$ (i.e. the case of external corrosion). For $-1<e<1$, the general case with both internal and external corrosion coexists. These parameters completely characterize the corroded ring. We develop a Python script in the Abaqus Python development environment to automatically generate the FE models after prescribing these parameters to allow extensive parametric analysis. We assign quite dense structural meshes (Fig. S9) to this model by element type CPS4 (a 4-node bilinear quadrilateral element in Abaqus). For boundary conditions we assign a symmetric boundary to the symmetric line to allow symmetric deformation only and, to exclude rigid body motion, the crown point of cross-section at $s=0$ is fixed by constraining all degrees of freedom. External pressure is imposed on the outer boundary (Fig. 3), the Riks step is used to follow the deformation path and geometric large displacement non-linearity is considered. Thus, external pressure is considered as a follower load. The material type is assumed to be linearly elastic with elastic modulus of 200 GPa (the same as steel) and a Poisson's ratio of 0.3.

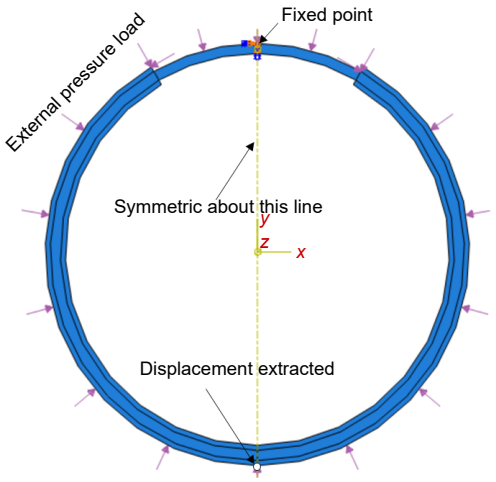

Fig. 3 Loading and boundary conditions of FEA

3.2 Load-displacement curve comparison

In FEA, as mentioned above, the crown-point is fixed and rigid body motion is thus excluded. Thus, we extract the displacement of the lowest point during deformation and now the vertical displacement of this point is equal to $w_1(0)+w_2(\pi)$ (the sum of two radial displacements at $s=0$ and $s=\pi$). By using the sum $w_1(0)+w_2(\pi)$, we exclude the effect of rigid-body motion, since the vertical rigid-body motion takes the form:

$$w_1|_{\text{rigid}}=b\cos s,\quad w_2|_{\text{rigid}}=b\cos s,$$
$$w_1|_{\text{rigid}}(0)+w_2|_{\text{rigid}}(\pi)=b(1-1)=0,$$

where $w_1|_{\text{rigid}}$ and $w_2|_{\text{rigid}}$ are the rigid-body-motion related radial displacements. Thus, the rigid-body motion's effect is cancelled in this sum. The physical meaning of this sum is also clear: if this sum is positive, then during deformation the lowest point and crown-point become closer; otherwise their distance apart increases. We can see that for different e, this sum may be positive or negative in the following.

In Fig. 4, we compare theoretical results (extensible and inextensible models) with the FEA results for $e=1$ (internal corrosion) and $e=-1$ (external corrosion) when $R_2=1.0$ m, the corrosion severity parameter $d=0.8$, $t_2/R_2=0.05$, and $s_1=\pi/6$. Even when $R_2/t_2=20$ (a relatively thin ring), the effect of e is evident. It affects the large deformation mode: for $e=-1$ at large deformation phase, as p increases $w_1(0)+w_2(\pi)$ increases and remains positive; however, for $e=1$, when p increases, it is negative at large deformation phases and it continuously decreases to a lower value. Both inextensible model and extensible model agree well with FEA results.

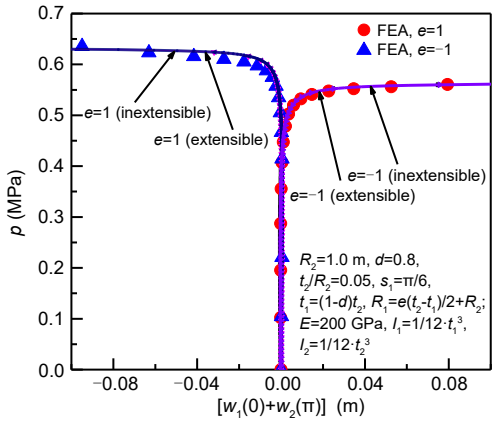

Fig. 4 Comparison of theoretical and FEA results for $e=1$ (internal corrosion) and $e=-1$ (external corrosion)

The situation is quite different when deformation is small, and in Fig. 5 we amplify the plots of Fig. 4 for a small deformation. In the case of $e=1$ (internal corrosion) when p starts to increase from zero, $w_1(0)+w_2(\pi)$ initially decreases to a negative value but, after p increases further, $w_1(0)+w_2(\pi)$ increases and approaches to zero. Finally, when p increases further, it changes its sign and becomes positive. In the case of

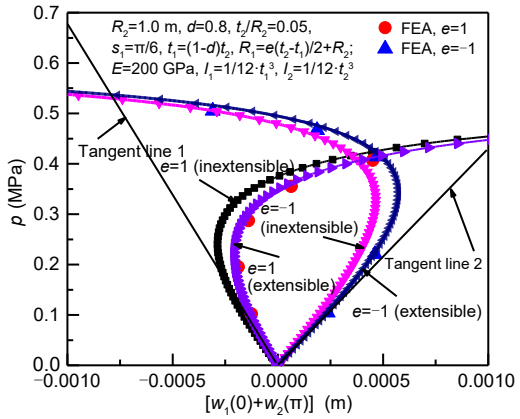

Fig. 5 Detailed comparison for initial deformations

e=−1 (external corrosion), the situation is in the opposite direction: initially $w_1(0)+w_2(\pi)$ increases to positive values, then it decreases to zero and finally becomes negative when p increases further. When deformation is small, the extensible model's result agrees with the FEA results better than that of the inextensible model, but the discrepancy is not so large. We found that the discrepancy becomes significantly larger when e=0 in the following interesting result. The tangent line 1 and tangent line 2 are just tangent lines of the extensible model's curves at point p=0 and are explicitly calculated by Eq. (9). When deformation increases, the discrepancy between the inextensible model and the extensible model decreases and almost vanishes as in Fig. 4.

Fig. 6 shows the special case e=0. Comparing the result with the ones from e=−1 or 1, we find that the pressure reaches high values when the deformation is significantly smaller. For example, in Fig. 4, if e=1

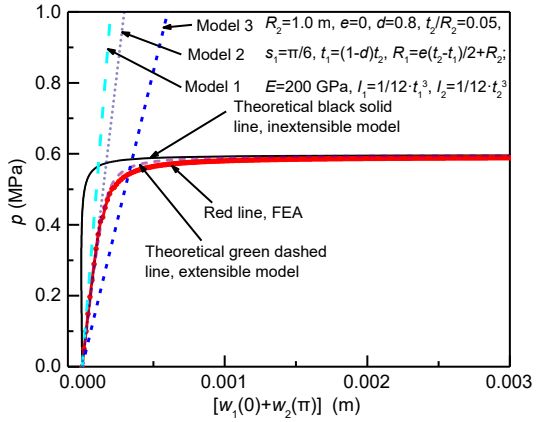

Fig. 6 Comparison for e=0 case (references to color refer to the online version of this figure)

the pressure still increases when $w_1(0)+w_2(\pi)$ is about 0.02 m. However, in Fig. 6 the pressure does not show significant increase when $w_1(0)+w_2(\pi)$ is about 0.001 m which is much smaller than the 0.02 m of the previous case. The discrepancy between the inextensible model and the extensible model becomes quite obvious: the solid black line (inextensible result) initially has a negative slope (i.e. when p starts to increase from 0, $w_1(0)+w_2(\pi)$ becomes negative initially) and the pressure seems to jump (steeply) to a high value when $w_1(0)+w_2(\pi)$ is extremely small (much smaller than the corresponding FEA and extensible results). The inextensible model does not agree well with the FEA results—at least during the initial deformation phase. In contrast, the extensible model agrees well with the FEA in that phase.

We formulate three models to calculate the initial slope as follows. Model 2's line is from initial slope calculation by Eq. (9). Model 3 is a simplified model: we assume no tangential displacement and that radial displacements are constant for both regions by applying formulas:

$$v_1'-w_1=-w_1=-w_1(0)=\frac{-pR_1\left(R_1+\frac{t_1}{2}\right)}{Et_1},$$

$$v_2'-w_2=-w_2=-w_2(\pi)=\frac{-pR_2\left(R_2+\frac{t_2}{2}\right)}{Et_2}.$$

The slope now is calculated by

$$\frac{p}{w_1(0)+w_2(\pi)}=\left[\frac{R_1\left(R_1+\frac{t_1}{2}\right)}{Et_1}+\frac{R_2\left(R_2+\frac{t_2}{2}\right)}{Et_2}\right]^{-1}.$$

Model 1 is also a simplified model: we disregard the corroded region and the slope is calculated as $p/\left[w_1(0)+w_2(\pi)\right]=\left[R_2(R_2+t_2/2)/(Et_2)\right]^{-1}$. Model 1 is equivalent to the radial contraction of uniform ring under pressure with thickness t_2 and radius R_2. We see that model 3 underestimates the slope and model 1 overestimates the slope. Only model 2 from delicate calculation of Eq. (9) fits well with FEA results. These comparisons show the effectiveness of initial slope calculation by Eq. (9).

We present the initial slope variation (by Eq. (9)) for various values of e in this thinner case t_2/R_2=0.05 in Fig. S10. Instead of presenting the initial slope directly, we present the reciprocal of this slope in this figure more conveniently. When e=−1 (external corrosion) the reciprocal $p^{-1}(w_1(0)+w_2(\pi))$ has a positive value, and when e increases this reciprocal decreases (equivalently the slope increases and the pressure increases more steeply during the initial deformation phase). When e increases to zero the reciprocal is still a positive value and, interestingly, the reciprocal decreases to zero when e is about 0.156 (the slope is thus infinity and it means that pressure suddenly jumps to a large value when $w_1(0)+w_2(\pi)$ is extremely small). When e just increases above 0.156, the reciprocal becomes negative and correspondingly the slope becomes negative infinity. When e increases further, the reciprocal decreases to lower negative values meaning that the slope becomes negative and smaller in magnitude in this case. This reciprocal-e curve seems to be approximately a straight line but it does not necessarily pass through the original point (0, 0). The magnitudes of the slopes at e=1 and e=−1 are not necessarily the same. For example, in the case of e=−1, the reciprocal is about 0.0023; however, at e=1, the reciprocal is about −0.0015. This shows the significant difference between internal corrosion and external corrosion.

We present similar comparisons for the thicker case where t_2/R_2=0.1 and d=0.5 in Fig. 7. In Fig. 7, the load-deformation curves are plotted for both theoretical results (extensible and inextensible) and FEA results. The overall agreement between both theoretical results and FEA results is good. Moreover, consistent with the above thinner case, when e=0 the increase of pressure in the initial deformation phase is quite steep and the extensible model predicts the FEA results better than the inextensible model. Similarly, e=1 and e=−1 have quite distinct large deformation phases. When e=−1, $w_1(0)+w_2(\pi)$ approaches lower negative values when p is large; however, when e=1, $w_1(0)+w_2(\pi)$ approaches higher positive values when p is large. When e=0, $w_1(0)+w_2(\pi)$ also approaches higher positive values when p is large. Fig. 8 shows the initial deformation results by amplifying the plots in Fig. 7. It is evident that for e=0 the inextensible model does not agree well with the FEA results and the extensible model predicts much better results. However, when e=−1, and 1, although the extensible model is more accurate, the discrepancy between the two models is slight. Three tangent lines in Eq. (9) approximate the FEA results well when p is small and the best approximation is attained for e=0. Comparing this with the result of the thinner case in Fig. 5, there is a fundamental difference. In the previous case for e=−1 the initial slope is negative, while at larger deformation phase, $w_1(0)+w_2(\pi)$ changes its sign and becomes positive. In direct contrast, in the case of e=−1 the initial slope is negative, but in the larger deformation phase there is no change of sign of $w_1(0)+w_2(\pi)$ and it remains negative.

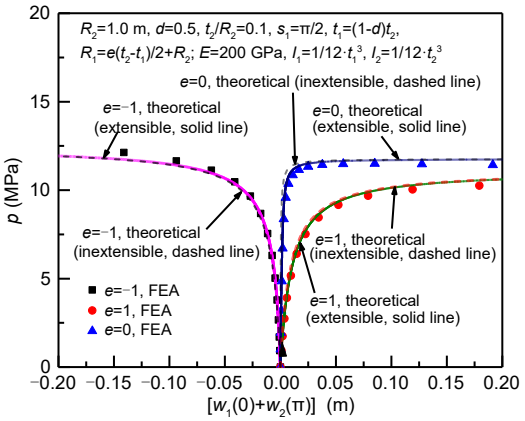

Fig. 7 Comparison for thicker case t_2/R_2=0.1

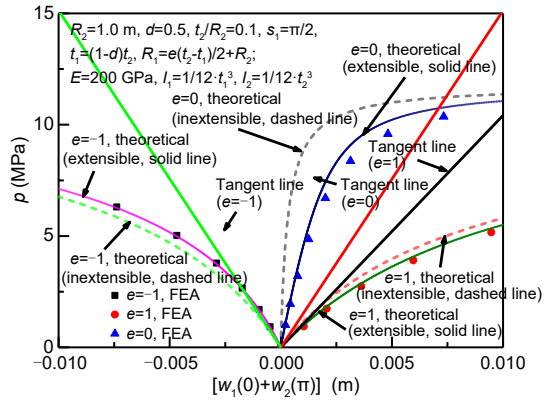

Fig. 8 Comparison of initial deformation in the thicker case

Fig. S11 presents the relationship between the reciprocal of initial slope by Eq. (9) and e for this thicker case. Comparing this figure with Fig. S10, there are distinct differences: when e=−1, the slope is negative, while in the previous case the slope is positive; similarly, when e=1, the slope is positive, while in the

previous case it is negative. In the following Section 4 we will show that this difference is highly related to the angular extent s_1. When e passes −0.278, the initial slope abruptly changes from minus infinity to positive infinity. We note that the magnitudes of the reciprocals of the initial slopes are quite different for e=−1 and e=1: at e=−1, the magnitude is about −0.0004, but at e=1, it is about 0.0010.

4 Parametric analysis

In this section, we present detailed parametric analysis of the initial slope and eigenvalue of the homogeneous version of this problem in Eq. (8). Our emphasis is on the effect of the misalignment parameter e. In the parametric analysis of the eigenvalue problems, we compare the results from two previously developed continuity conditions in Eqs. (5) and (6).

4.1 Initial slope analysis

Since we have shown previously that the extensible model should be used instead of the inextensible model for accurately predicting the initial slope, only the extensible model from Eq. (9) will be used.

4.1.1 Effect of relative defect depth d

Fig. 9a presents the relationship between the initial slope and parameters d and e when s_1=π/2 and t_2/R_2 =0.1 are fixed (initial slope represents the slope of tangent to the pressure-displacement curve at zero pressure representing the stiffness of the structure when pressure is well below the critical collapse pressure). The pressure $\tilde{p}$ means the pressure normalized by the first bifurcation pressure of a uniform ring of thickness t_2 and radius R_2. When e=1.0, 0.8, 0.6, 0.4, 0.2, and 0.0, as d increases, $\tilde{w}/\tilde{p}$ (where $\tilde{w}$ means the normalized displacement defined as $(w_1(0)+w_2(\pi))/R_2$) increases and approaches infinity when $d\to 1^-$ (approaching from below). However, when e=−0.2, $\tilde{w}/\tilde{p}$ first increases and then decreases to a negative value when d is about 0.6. It decreases further to a minimum negative value and then increases to infinity when $d\to 1^-$. When e=−0.4, −0.6, −0.8, and −1.0, the trends are similar: $\tilde{w}/\tilde{p}$ always decreases until d reaches about 0.9 and then increases to positive infinity when $d\to 1^-$. This figure also shows that e=0 is not that special and

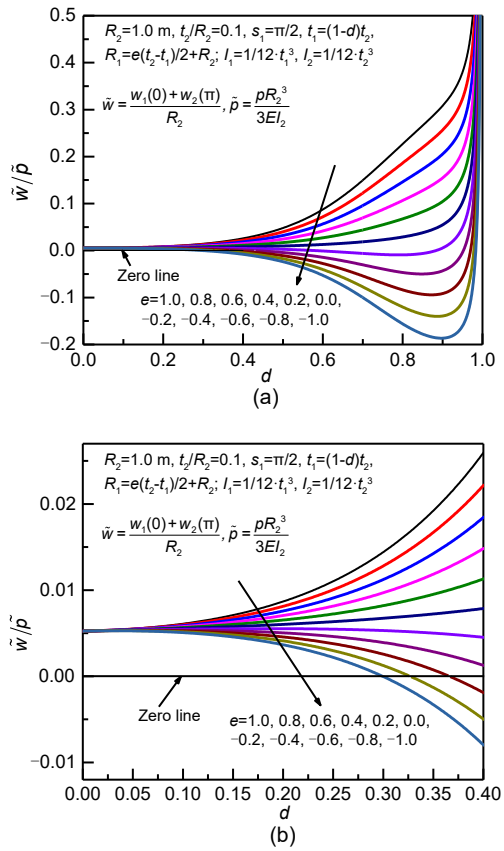

Fig. 9 Reciprocal of initial slope versus d for various e (a) and amplified plots for smaller d (b)

indeed the $\tilde{w}/\tilde{p}$ curve is closest to the zero line when e=−0.2. Fig. 9b shows amplified plots for smaller d: when d<0.3, $\tilde{w}/\tilde{p}$ remains positive.

The situation seems significantly different when s_1=π/6 in Fig. 10a. Fig. 10b shows the overall variation of $\tilde{w}/\tilde{p}$ when d increases. For e=1.0, 0.8, 0.6, 0.4, and 0.2 the trends are similar. As d increases, $\tilde{w}/\tilde{p}$ first decreases from a positive value to a negative value and then increases to positive infinity when $d\to 1^-$. However, when e=−1.0, −0.8, −0.6, −0.4, and −0.2, as d increases from 0 to about 0.8, $\tilde{w}/\tilde{p}$ first slowly increases to a maximum point and then decreases rapidly to zero, while when d further increases, $\tilde{w}/\tilde{p}$ decreases further to a minimum value and then increases to positive infinity when $d\to 1^-$. Since as $d\to 1^-$ the corroded region has a very small remaining thickness t_1 and the stiffness of the intact region is much larger than the stiffness of the corroded region, it is equivalent to the intact region remaining undeformed and that all deformation is confined to the corroded region. From this

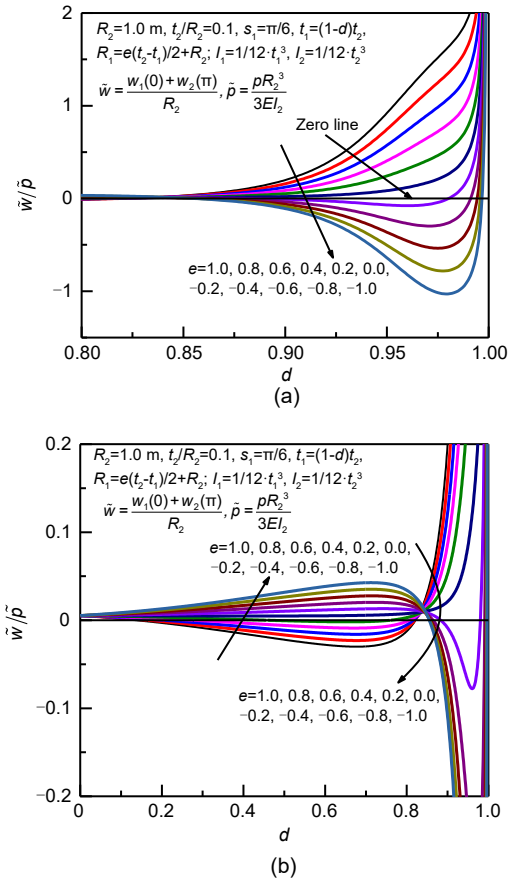

Fig. 10 Reciprocal of initial slope versus d for various e when s_1=π/6: (a) d ranging from 0.8 to 1.0; (b) d ranging from 0 to 1.0

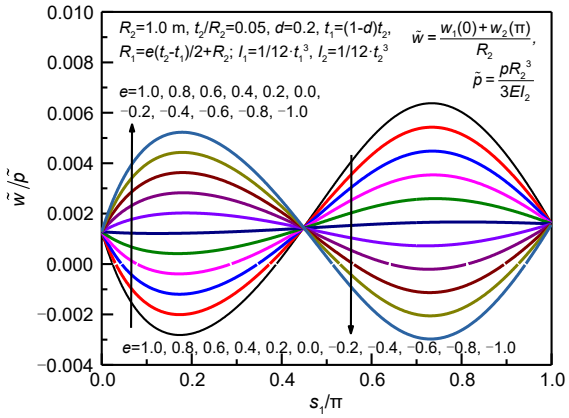

Fig. 11 Dependency of $\tilde{w}/\tilde{p}$ on s_1 for t_2/R_2=0.05 and d=0.2

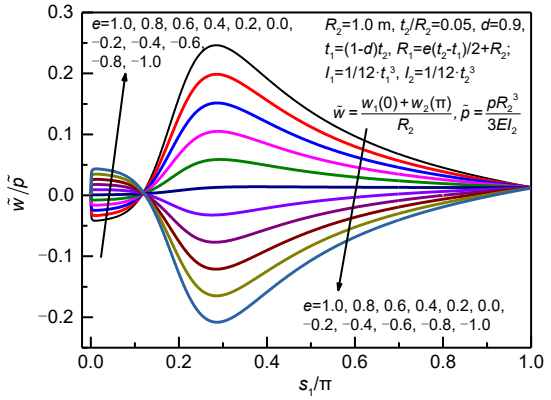

Fig. 12 Dependency of $\tilde{w}/\tilde{p}$ on s_1 for t_2/R_2=0.05 and d=0.9

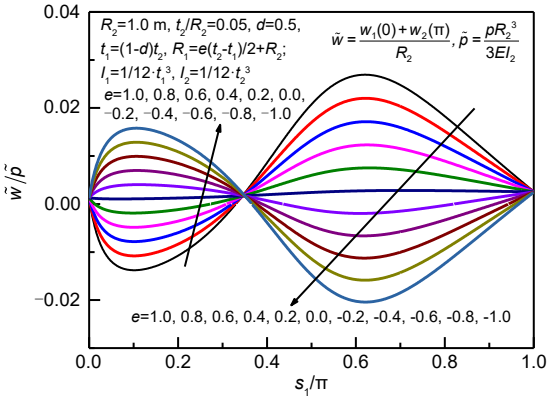

Fig. 13 Dependency of $\tilde{w}/\tilde{p}$ on s_1 for t_2/R_2=0.05 and d=0.5

perspective the corroded region behaves as a uniform arch under external pressure with both ends fixed. And the result that $\tilde{w}/\tilde{p}$ approaches to positive infinity instead of negative infinity is equivalent to this uniform arch under pressure having its crown point displaced inward towards the arch center (Yan et al., 2018a). The above analysis seems to suggest the important role of s_1.

4.1.2 Effect of angular defect size s_1

Figs. 11–13 show the dependency of $\tilde{w}/\tilde{p}$ on s_1 and e. For smaller d=0.2 in Fig. 11, when e=1.0, 0.8, 0.6, 0.4, and 0.2 as s_1 increases from 0 to π, $\tilde{w}/\tilde{p}$ first decreases from a positive value to a negative minimum value when s_1/π is about 0.2, it then increases monotonically to a positive maximum when s_1/π is about 0.75 and finally decreases to a small positive value. When e=−0.2, −0.4, −0.6, −0.8, and −1.0, the situation is quite different: $\tilde{w}/\tilde{p}$ first increases to a positive maximum, then decreases to minimum (not necessarily negative) and finally increases to a small positive value. The reader may be wondering why, at s_1=0, π, $\tilde{w}/\tilde{p}$ is positive: this is a direct consequence of uniform membrane compression of the uniform ring under external pressure. At $s_1/\pi\approx$0.45 all curves seem to coincide with small $\tilde{w}/\tilde{p}$ value, although these curves

are indeed not intersecting exactly at the same point as can be seen in a careful check of a locally amplified plot in Fig. S12. In Fig. S12, we present a detailed result around s_1=0.45 and indeed all curves do not intersect at the same point, but the points of intersection form a small triangle-shaped region with s_1 ranging from 0.447 to 0.451 and $\tilde{w}/\tilde{p}$ ranging from 0.0014 to 0.00145. Fig. 12 presents the results for d=0.9, meaning that the thickness of the corroded region is only 10.0% of the thickness of the intact region. This severity of corrosion makes this result quite distinct. When s_1 is about 0.0 all curves abruptly jump, and at about s_1=0.13 all curves have small $\tilde{w}/\tilde{p}$ values (consistent with the previous case of d=0.2 but here s_1 is much smaller). Curves of e=1.0, 0.8, 0.6, 0.4, and 0.2, all increase to a positive maximum and then decrease to a small value when $s_1 \to \pi$. By contrast, curves of e=−0.2, −0.4, −0.6, −0.8, and −1.0 decrease to a minimum negative value and then increase to a small value at $s_1 \to \pi$. Similarly, Figs. 13 and S13 present the related results for mild corrosion d=0.5. All curves have similar trends as above when d=0.9 and 0.2 but, at $s_1 \approx 0.35$, all curves have small $\tilde{w}/\tilde{p}$. The above discussion suggests that s_1, around which point all curves have small $\tilde{w}/\tilde{p}$, is decreasing from 0.5 to 0.0 when d increases from 0 to 1. These characteristic s_1 points seem not to have been previously reported.

4.2 Eigenvalue analysis

The problem by Eq. (8) with boundary conditions $w_1'(0)=w_2'(\pi)=0$ and continuity conditions in Eq. (5) or Eq. (6) is an eigenvalue problem, and these solutions offer an opportunity to study the effect of choice of continuity conditions.

Fig. 14 presents the dependency of the lowest non-zero eigenvalue p for various values of d and e (note that p=0 is also an eigenvalue related to the rigid-body vertical translation and is disregarded). Again $\tilde{p}=pR_2^3/(3EI_2)$ describes the relative stiffness of a corroded ring when compared with an intact uncorroded ring. $\tilde{p}|_{e=0}$ is $\tilde{p}$ when e=0 (the symmetric corrosion case). At e=0, both the simplified condition (Eq. (8)) and the full condition (Eq. (5)) coincide since $R_1=R_2$ in this case. Thus, the result is presented in terms of $\tilde{p}/\tilde{p}|_{e=0}$ to emphasize the influence of e. Dashed lines represent full formulation by Eq. (5) and solid lines represent simplified formulation by Eq. (8). As e ranges

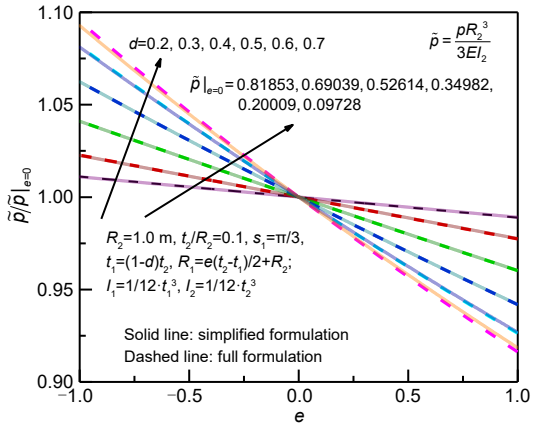

Fig. 14 Lowest Eigenvalue comparison for various d and e when t_2/R_2=0.1 and s_1=π/3

from −1 to 1, for all d, $\tilde{p}/\tilde{p}|_{e=0}$ is monotonically decreasing almost linearly. When d=0.2, its value changes from about 1.01 to about 0.99. When d=0.7, its value changes from about 1.09 to 0.92. This shows that as d increases, the effect of e increases. Of course, when d=0.2, 0.3, 0.4, 0.5, 0.6, and 0.7, $\tilde{p}|_{e=0}$ values decrease as 0.81853, 0.69039, 0.52614, 0.34982, 0.20009, and 0.09728, and this means that the increase of corrosion severity d reduces the bifurcation pressure. The discrepancy between dashed lines and solid lines is very small and is only notable when d=0.7.

Fig. 15 presents the results when t_2/R_2=0.05 where the ring is thinner: dashed lines agree well with solid lines and, for d=0.7, $\tilde{p}/\tilde{p}|_{e=0}$ changes from about 1.04 to about 0.96. Comparison with Fig. 14 shows that the effect of e decreases when the ring becomes thinner.

Fig. 16 presents the results with t_2/R_2=0.1 and s_1=2π/3 (twice the s_1 in previous Fig. 14). By comparison

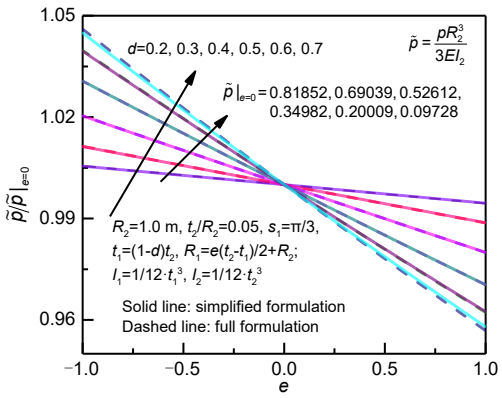

Fig. 15 Lowest eigenvalue comparison for various d and e when t_2/R_2=0.05 and s_1=π/3

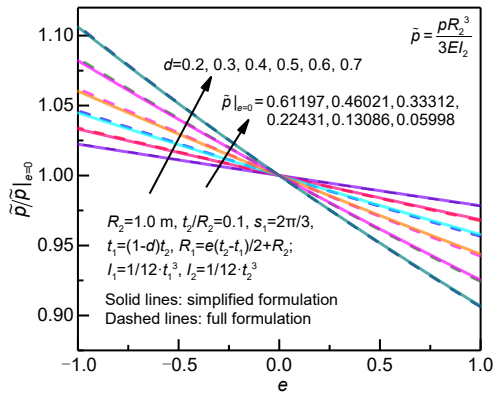

Fig. 16 Lowest eigenvalue comparison for various d and e with t_2/R_2=0.1 and s_1=2π/3

with Fig. 14 the effect of e is only slightly increased. For example for d=0.7, when e ranges from −1 to 1, $\tilde{p}/\tilde{p}|_{e=0}$ changes from about 1.11 to about 0.91.

Fig. 17 presents the results of the effect of s_1 and e when t_2/R_2=0.1 and d=0.5. As e increases, similarly $\tilde{p}/\tilde{p}|_{e=0}$ decreases almost linearly. When $s_1=\pi/10$ the corrosion region is quite narrow and the effect of e is small. However, when s_1 increases to 3π/10, the effect of e increases significantly. When s_1 is further increased to 7π/10, the effect of e is only slightly increased. Finally, when s_1=9π/10, and e ranges from −1 to 1, $\tilde{p}/\tilde{p}|_{e=0}$ ranges from about 1.08 to about 0.93.

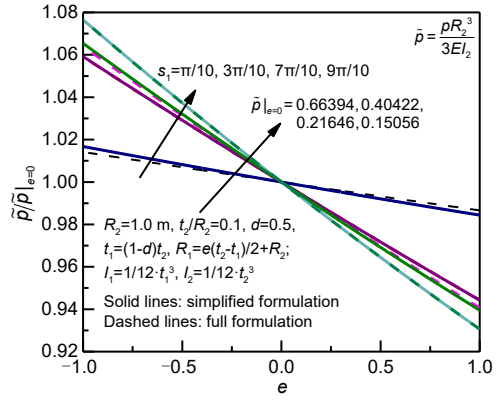

Fig. 17 Lowest eigenvalue comparison for various d and e with t_2/R_2=0.1 and d=0.5

From all previous analyses, we conclude that when s_1 is smaller and d is larger, the discrepancy between simplified and full formulations is larger, but for all cases the discrepancy leads to a very small error.

In Table S2, we explicitly present some critical pressure comparisons for the simplified continuity condition and the full continuity condition. In the first case ('simplified 1' and 'full 1'), the geometric parameters are d=0.5, $s_1=\pi/2$, and t_2/R_2=0.1. In the second case ('simplified 2' and 'full 2') the geometric parameters are d=0.8, $s_1=\pi/6$, and t_2/R_2=0.15. In the third case ('simplified 3' and 'full 3') the geometric parameters are d=0.2, $s_1=\pi/3$, and t_2/R_2=0.1. All pressure values are normalized by $3EI_2/R_2^3$ (i.e. $\tilde{p}$). 'Error 1', 'Error 2', and 'Error 3' are the relative errors between the critical pressures in the full and simplified formulations. From Table S2, the maximum error occurs when e=1 for the first case and the maximum error has magnitude 0.19544%. For the other two cases, the relative error is at most 0.02176%. This detailed comparison shows the very slight influence of choice between Eqs. (5) and (6) which fact justifies the use of the simpler Eq. (6) throughout this paper except in this section.

5 Infallible perturbation method

In previous sections, the corrosion depth is constant in the corroded region, and in Section 5 we solve for the case where the corrosion depth is varying. Chen et al. (2021a) published the so-called homotopy analysis method (HAM) to solve the bifurcation pressure of corroded rings. Illuminated by that work, we present a more straightforward approach using the Lyapunov artificial small-parameter method and show that the two methods give identical results although the Lyapunov method seems more direct. We show rigorously that this method is always valid since the power series constructed always converges. Only homogeneous equations are solved in the paper by Chen et al. (2021a), however, in this section, we have solved both the inhomogeneous equation by Eq. (1) (only the inextensible case with simplified continuity condition by Eq. (6) is solved to simplify the illustration) and the homogeneous equations by Eq. (8) for arbitrary thickness distribution function $t(s)$ and middle axis radius distribution $R(s)$ for $s\in[0, \pi]$. The more general equation of Eq. (1) for any $t(s)$ and $R(s)$ is:

$$\frac{EI(s)(w''(s)+w(s))}{R^2(s)}+\frac{p(-4R^2(s)+t^2(s))}{8}+pR(s)w(s)=C, \tag{10}$$

where R and t are functions of $s\in[0, \pi]$. C is a constant and this equation is specialized to the original Eq. (1) by requiring that $R(s)$ and $t(s)$ are piecewise constants and jump at $s=s_1$ only, and w is defined on $[0,\pi]$ (radial displacements) and the boundary conditions are $w'(0)=w'(\pi)=0$, $\int_{[0,\pi]} w=0$. $I(s)=1/12\cdot t^3(s)$ of course. The homogeneous version of this equation is just:

$$\frac{EI(s)(w''(s)+w(s))}{R^2(s)}+pR(s)w(s)=C. \quad (11)$$

To use Lyapunov arbitrary small-parameter method, we need to plug in an artificial parameter ε to these equations to transform Eq. (11) into:

$$w''(s)+\varepsilon\left(w(s)+pR^3(s)w(s)-\frac{CR^2(s)}{EI(s)}\right)=0. \quad (12)$$

Transforming Eq. (10) into:

$$w''(s)+\varepsilon\left\{w(s)+pR^3(s)w(s)-\frac{CR^2(s)}{EI(s)}-\frac{1}{8}\cdot\frac{pR^2}{EI(s)}\cdot(4R^2(s)-t^2(s))\right\}=0, \quad (13)$$

then we assume that w can be expanded into a power series of ε as

$$w=w_0+\varepsilon w_1+\varepsilon^2 w_2+\cdots. \quad (14)$$

After the calculation of w_0, w_1, $\cdots$, we set $\varepsilon=1$ to restore the original equation Eqs. (10) and (13). Substituting it into Eq. (13), it yields:

$$w_0''=0, \quad (15)$$

$$w_1''=-w_0-\frac{pR^3w_0}{EI}+\frac{CR^2}{EI}-\frac{1}{8}\cdot\frac{pR^2}{EI}\cdot(t^2-4R^2), \quad (16)$$

$$w_i''=-w_{i-1}-\frac{pR^3w_{i-1}}{EI},\quad i\geqslant 2. \quad (17)$$

If it is substituted into the homogeneous equation Eq. (12), we only need to replace Eq. (16) by $w_1''=-w_0-pR^3w_0/(EI)+CR^2/(EI)$. Then $w_0''=0$ leads to $w_0=as+b$ for some constants a and b, since a and b are completely unknown, without loss of generality, we may require $w|_{s=0}=w_0|_{s=0}=b$ and $w'|_{s=0}=w_0'|_{s=0}=a$. Note that $w'(0)=0$ is a boundary condition and thus $a=0$ in this case. So there are only two undetermined constants C and b. For the homogeneous case, direct integration twice yields:

$$w_i(s)=\int_{[0,s]}\int_{[0,s]}\left\{-w_{i-1}(\tau)-\frac{pR^3(\tau)w_{i-1}}{EI(\tau)}\right\}\mathrm{d}\tau\mathrm{d}s,\ i\geqslant 2, \quad (18)$$

where the two integration constants are zero since $0=w'|_0-w_0'|_0=\varepsilon w_1'|_0+\varepsilon^2 w_2'+\cdots\Rightarrow w_i'|_0=0,\ \forall i\geqslant 1$; $0=w|_0-w_0|_0=\varepsilon w_1|_0+\varepsilon^2 w_2+\cdots\Rightarrow w_i|_0=0,\ \forall i\geqslant 1$.

Then if we simplify the notation by defining $Q(s)=1+pR^3(s)/EI(s)$, the explicit solution of $w_i(s)$ is:

$$w_i=\iint Q\cdot\iint Q\cdot\iint Q\cdots\iint(Q\cdot w_1),\ i\geqslant 2, \quad (19)$$

where by definition $\iint f$ is a mapping which maps s to $\int_{[0,s]}\int_{[0,s]} f(\tau)\mathrm{d}\tau\mathrm{d}s$ for any function f and there are $i-1$ $\iint$ operations. It follows that

$$\max_{s\in[0,\pi]}|w_i(s)|\leqslant\left(\max_{s\in[0,\pi]}|Q(s)|\right)^{i-1}\cdot\max_{s\in[0,\pi]}|w_1(s)|\cdot\iint\cdots\iint 1=\left(\max_{s\in[0,\pi]}|Q(s)|\right)^{i-1}\cdot\max_{s\in[0,\pi]}|w_1(s)|\cdot\frac{\pi^{2i-2}}{(2i-2)!}. \quad (20)$$

Thus, from elementary functional analysis, the power series for ε, $w=w_0+\varepsilon w_1+\varepsilon^2 w_2+\varepsilon^3 w_3+\cdots$, has convergence radius of infinity, and then the power series is always convergent for any real number ε. We note that, during the integrations, there are two unknown constants remaining and thus the final expression of w contains these two unknowns C and b. However, there are still two conditions to be imposed: $w'(\pi)=0$ and $\int_{[0,\pi]} w=0$. By imposing these two conditions there are two conditions and two unknowns C, b. In the homogeneous case, they are linear in C, b and thus define an eigenvalue problem (the characteristic equation of some resulting matrix by equating determinant

to zero is formulated and solved) which is easily solved. While for the inhomogeneous case, C, b can be calculated by matrix inversion.

If in Eq. (12), we decompose as $w''(s)=(1-\varepsilon)w''(s)+\varepsilon w''(s)$, move $(1-\varepsilon)w''$ to the other hand side of the equation, replace the symbol ε by symbol q and carry out expansion by q, then this is just the so-called HAM method in the recent paper (Chen et al., 2021a). So in this paper, the HAM method is just the same as the Lyapunov small-parameter method although the latter method seems more straightforward. However, the HAM method has an additional convergence controlling parameter c_0 and this aspect is discussed in ESM E. In ESM E, we show that in general if $c_0\in(-2, 0)$ the related power series always converges by some mathematical analysis of analyticity, and even if c_0 is slightly greater than 0 or slightly lower than -2 the power series may diverge rapidly (note that $c_0=-1$ is implicitly assigned in Eqs. (12) and (13), and thus convergence is guaranteed).

Note that in the above methods only integrations are necessary, but it is well-known that exact integration is only possible for some simple types of functions. Thus, we propose to first approximate the functions by polynomials on $[0, \pi]$ and it is well-known that by the Weierstrass theorem each continuous function on $[0, \pi]$ can be approximated by some polynomials with an arbitrarily small error. By first approximation by polynomials, we can carry out integrations trivially and exactly. We present some examples in the following.

5.1 Eigenvalue solution of homogeneous equations

As an example, we assign $R(s)=1+0.1s$ and $(EI)^{-1}=1+0.1s$. In the above, we have shown that, in the homogeneous case, by truncating the series $w=w_0+w_1+w_2+\cdots$ to $w=w_0+w_1+\cdots+w_m$ for some m, prescribing the conditions $w'(\pi)=0$ and $\int_{[0,\pi]} w=0$ leads to a matrix (whose entry is some function of p) eigenvalue problem with two unknowns C, b. This eigenvalue problem can be solved by equating the determinant of this matrix to zero to obtain the so-called characteristic equation of variable p. Then the root of p is obtained.

Fig. 18 represents the determinant (Det) of the matrix for various truncation numbers m. For m=2, 4, and 6, there are no roots for $p\in[0, 2]$ and as m becomes large, the curves converge and their roots also converge to the true value of root p. For the curves of

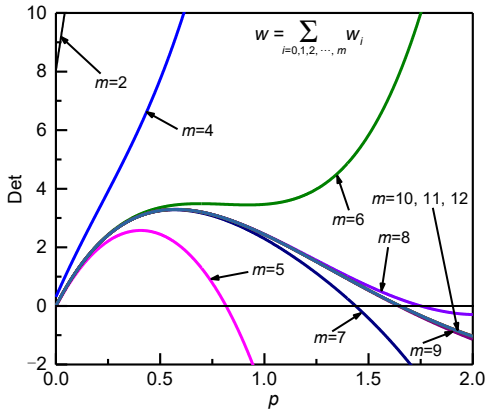

Fig. 18 Characteristic equations for different m

m=5, 7, 8, 9, 10, 11, and 12 the characteristic equation has some roots. And for each curve, corresponding to each root, we can calculate the matrix's eigenvectors for C, b and substitute the calculated C, b back into the expression $w=w_0+w_1+w_2+\cdots+w_m$ to obtain the characteristic eigenfunctions (modal shapes).

Fig. 19 shows how the modal shape evolves when the truncation number m is increased. It is evident that as m increases, the modal shape converges fast. We have also compared the above results with the numerical results by the shooting method and their agreement is almost exact when m=12 (see ESM F for the numerical shooting methods to solve both Eqs. (10) and (11)).

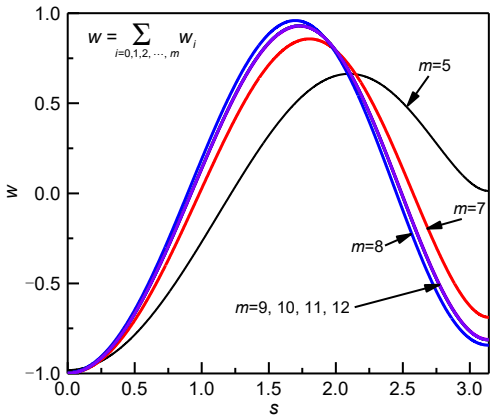

Fig. 19 Mode shapes of eigenfunctions for different m

5.2 Inhomogeneous problem's solution

If $R(s)=1$ but $t(s)=1+0.1\cos s$ and $(EI)^{-1}=t^3(s)$, exact integrations are difficult, so we first use polynomial approximation of $t(s)$ and $(EI)^{-1}$ by power series expansion to s^{10}-order as:

$(EI)^{-1}\approx 0.75064+0.0047099s+\cdots+0.0000330294s^{10}$,
$t\approx 1.1-0.05s^2+0.0041667s^4+\cdots-2.7557\times10^{-8}s^{10}$.

Substituting these polynomial approximations into Eqs. (16) and (17), the integrations can then be exactly calculated.

Fig. 20 presents a comparison with numerical solutions by the shooting method. The red dashed line is the numerical solution. The truncated series $w=w_0+w_1+\cdots+w_m$ for m=5, 7, 8, and 12 is presented. It is evident that when m=12, the numerical solution and the perturbative solution agree well and as p increases, $w(0)+w(\pi)$ is negative and decreases. This example shows the effectiveness of a perturbation solution in solving inhomogeneous equations.

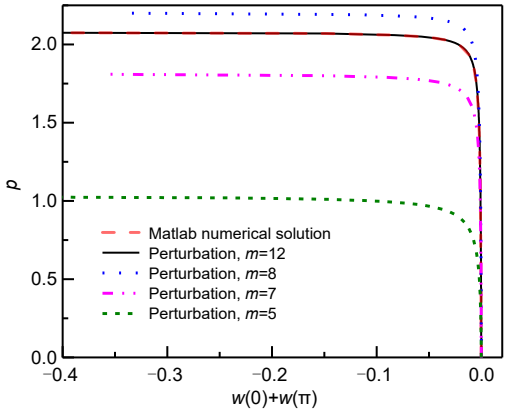

Fig. 20 Comparison with numerical results (references to color refer to the online version of this figure)

6 Conclusions

1. The derived inhomogeneous formulation's load-displacement curve agrees well with the FEA results.

2. The misalignment parameter e significantly affects the deformation paths even when the ring is thin (e.g. t_2/R_2=0.05).

3. The rigorous adoption of the Euler-Bernoulli beam assumption leads to a complex continuity condition equation (derived in ESM C); however, a comparison analysis shows that the simplified continuity condition, by simply requiring no abrupt jump of tangential displacements, yields almost identical results with only a very small error.

4. The initial deformation is highly affected by membrane extensibility, and the perturbative solution in this paper (ESM D) is unexpectedly non-trivial and agrees well with the FEA predictions.

5. An initial slope calculation shows that e=0 is not necessarily the initially stiffest case. By an example, we show that the initial slope may be infinity when e is −0.278, i.e. e=0 is not special (Section 3.2). Unexpectedly, for some value of s_1 (the corrosion region's angular extent), the initial slope curves (Fig. 13) almost coincide for any e.

6. The semi-analytical procedure by the Lyapunov small-parameter method leads to convergent power series with infinite convergence radius and is suitable for solution of both homogeneous and inhomogeneous equations. In order to carry out integration exactly, we propose to first approximate the functions by polynomials and then carry out integration trivially (this approximation is always possible by the Weierstrass theorem that asserts that any continuous function on compact interval can be approximated arbitrarily accurately by polynomials). By mathematical analysis of function analyticity, we show definitely that the controlling convergence c_0 in the homotopy analysis method should be in (−2, 0) to guarantee convergence and thus we conclude there is no necessity to assign a $c_0\neq-1$ (ESM E).

7. In ESM G, we show a possible application of our theoretical result even when plasticity is present. The theoretical result is indeed useful when coupled with some plasticity criterion to predict collapse pressure in cases where a plasticity effect cannot be ignored.

The effect of plasticity may be included by tangent modulus method and may be subject to further research in the near future.

Acknowledgments

This work is supported by the Natural Science Foundation of Zhejiang Province (No. LQ21E050001), the Science and Technology Plan Project of Zhejiang Bureau of Quality and Technical Supervision (No. 20200307), and Eyas Program Incubation Project of Zhejiang Provincial Administration for Market Regulation (No. CY2022221) China.

Author contributions

Sun-ting YAN acquired the fund for this research, designed the research, derived the equations and theories, conducted FEA, wrote the draft, and made the revision. Ping TANG, Zhang-wei LING, and Yong-gui CHEN reviewed the manuscript and provided advice on writing and data analysis.

Conflict of interest

Sun-ting YAN, Ping TANG, Zhang-wei LING, and Yong-gui CHEN declare that they have no conflict of interest.

References

ASME (American Society of Mechanical Engineers), 2010. Rules for Construction of Pressure Vessels. Boiler and Pressure Vessel Code Section VIII Division 2., ASME.

Chen YF, Dong SH, Zang ZP, et al., 2021a. Buckling analysis of subsea pipeline with idealized corrosion defects using homotopy analysis method. *Ocean Engineering*, 234: 108865. https://doi.org/10.1016/j.oceaneng.2021.108865

Chen YF, Dong SH, Zang ZP, et al., 2021b. Collapse failure and capacity of subsea pipelines with complex corrosion defects. *Engineering Failure Analysis*, 123:105266. https://doi.org/10.1016/j.engfailanal.2021.105266

Fatt MSH, 1999. Elastic-plastic collapse of non-uniform cylindrical shells subjected to uniform external pressure. *Thin-Walled Structures*, 35(2):117-137. https://doi.org/10.1016/S0263-8231(99)00021-X

Fraldi M, Guarracino F, 2011. An improved formulation for the assessment of the capacity load of circular rings and cylindrical shells under external pressure. Part 1. Analytical derivation. *Thin-Walled Structures*, 49(9):1054-1061. https://doi.org/10.1016/j.tws.2011.03.014

Fraldi M, Guarracino F, 2013. Towards an accurate assessment of UOE pipes under external pressure: effects of geometric imperfection and material inhomogeneity. *Thin-Walled Structures*, 63:147-162. https://doi.org/10.1016/j.tws.2012.10.007

Gong SF, Zhou LB, Wang XP, et al., 2020. On the influence of interacting dual defects on the collapse pressure of pipes under external pressure. *Thin-Walled Structures*, 157:107140. https://doi.org/10.1016/j.tws.2020.107140

Gong SF, Zhou LB, Wang XP, et al., 2021. On the collapse of thick-walled pipes with corrosion defects under external pressure. *Marine Structures*, 76:102925. https://doi.org/10.1016/j.marstruc.2020.102925

Kyriakides S, Corona E, 2007. Mechanics of Offshore Pipelines. Volume I: Buckling and Collapse. Elsevier, Amsterdam, the Netherlands. https://doi.org/10.1016/B978-0-08-046732-0.X5000-4

Liao SJ, 2009. Notes on the homotopy analysis method: some definitions and theorems. *Communications in Nonlinear Science and Numerical Simulation*, 14(4):983-997. https://doi.org/10.1016/j.cnsns.2008.04.013

Liao SJ, 2012. Homotopy Analysis Method in Nonlinear Differential Equations. Higher Education Press, Beijing, China, p.153-165. https://doi.org/10.1007/978-3-642-25132-0

Netto TA, 2009. On the effect of narrow and long corrosion defects on the collapse pressure of pipelines. *Applied Ocean Research*, 31(2):75-81. https://doi.org/10.1016/j.apor.2009.07.004

Netto TA, Ferraz US, Botto A, 2007. On the effect of corrosion defects on the collapse pressure of pipelines. *International Journal of Solids and Structures*, 44(22-23): 7597-7614. https://doi.org/10.1016/j.ijsolstr.2007.04.028

Shen XL, Yan ST, Wang F, et al., 2016. On collapse failure analysis of subsea corroded sandwich pipelines under external pressure. *OCEANS MTS/IEEE Monterey*, p.1-8. https://doi.org/10.1109/OCEANS.2016.7761340

Teixeira AP, Palencia OG, Soares CG, 2019. Reliability analysis of pipelines with local corrosion defects under external pressure. *Journal of Offshore Mechanics and Arctic Engineering*, 141(5):051601. https://doi.org/10.1115/1.4042384

Timoshenko SP, Gere JM, 1961. Theory of Elastic Stability. McGrawHill-Kogakusha Ltd., Tokyo, Japan, p.109-152.

Wu H, Zhao HS, Li X, et al., 2021. A semi-analytical approach to elastic–plastic buckling analysis of pipes with asymmetric local wall thinning. *Thin-Walled Structures*, 162:107615. https://doi.org/10.1016/j.tws.2021.107615

Xue J, Fatt MSH, 2002. Buckling of a non-uniform, long cylindrical shell subjected to external hydrostatic pressure. *Engineering Structures*, 24(8):1027-1034. https://doi.org/10.1016/S0141-0296(02)00029-9

Xue JH, 2008. Asymptotic analysis for buckling of undersea corroded pipelines. *Journal of Pressure Vessel Technology*, 130(2):021705. https://doi.org/10.1115/1.2894293

Yan ST, Shen XL, Jin ZJ, 2015. On instability failure of corroded rings under external hydrostatic pressure. *Engineering Failure Analysis*, 55:39-54. https://doi.org/10.1016/j.engfailanal.2015.05.005

Yan ST, Shen XL, Jin ZJ, et al., 2016. On elastic-plastic collapse of subsea pipelines under external hydrostatic pressure and denting force. *Applied Ocean Research*, 58: 305-321. https://doi.org/10.1016/j.apor.2016.04.007

Yan ST, Shen XL, Chen ZF, et al., 2017. On buckling of non-uniform shallow arch under a central concentrated load. *International Journal of Mechanical Sciences*, 133: 330-343. https://doi.org/10.1016/j.ijmecsci.2017.08.046

Yan ST, Shen XL, Chen ZF, et al., 2018a. Collapse behavior of non-uniform shallow arch under a concentrated load for fixed and pinned boundary conditions. *International Journal of Mechanical Sciences*, 137:46-67. https://doi.org/10.1016/j.ijmecsci.2018.01.005

Yan ST, Shen XL, Jin ZJ, 2018b. Instability of imperfect non-uniform shallow arch under uniform radial pressure for pinned and fixed boundary conditions. *Thin-Walled Structures*, 132:217-236. https://doi.org/10.1016/j.tws.2018.08.018

Yan ST, Shen XL, Chen ZF, et al., 2018c. Symmetric

snap-through and equal potential energy load of non-uniform shallow arch under a concentrated load considering imperfection effect. *International Journal of Mechanical Sciences*, 146-147:152-179. https://doi.org/10.1016/j.ijmecsci.2018.07.037

Ye H, Yan ST, Jin ZJ, 2016. Collapse of corroded pipelines under combined tension and external pressure. *PLoS One*, 11(4):e0154314. https://doi.org/10.1371/journal.pone.0154314

Yu JX, Wang HK, Fan ZY, et al., 2017. Computation of plastic collapse capacity of 2D ring with random pitting corrosion defect. *Thin-Walled Structures*, 119:727-736. https://doi.org/10.1016/j.tws.2017.07.025

Electronic Supplementary Materials

ESMs A–G; Figs. S1-S18; Tables S1 and S2